

COMPUTATION OF LANDAU LEVELS AND SHUBNIKOV-DE HAAS OSCILLATIONS IN QUANTUM HETEROSTRUCTURES

BRUNO BUIJTENDORP



Bachelor Thesis

Submitted for the degree of Bachelor of Science (BSc)

Supervised by Michael Wimmer, Sebastian Rubbert, Anton Akhmerov

Theoretical Physics Group

Department of Quantum Nanoscience

Delft University of Technology

November 2016

ABSTRACT

We develop a computational method that can efficiently simulate Landau levels in quantum heterostructures, by reducing the problems dimensionality. We then apply this to a GaSb/InAs/AlSb broken gap quantum well in the trivial and inverted regimes. This heterostructure can be tuned into a 2DTI phase, and has possible applications in topological quantum computing. In the Landau fan of the inverted regime we observe the hole band shifting into the electron band, and an electron state crossing the gap to the hole band and vice versa. In the trivial regime we study the magnetic oscillations in the density of states near the Fermi energy, and observe a pronounced beating for a broadening of 0.3 meV.

ACKNOWLEDGMENTS

I would like to express my gratitude to Michael Wimmer for his professional guidance, and for providing me with valuable criticisms that have always been friendly and helpful. Furthermore, I want to show my great appreciation and thankfulness to Sebastian Rubbert, who has been very generous with his time for me, and from who I have learned a lot throughout the course of this project. I also want to express my gratefulness to Anton Akhmerov for always looking ahead and inspiring me to bring the project to a higher level. I am very thankful for his valuable insights. I am also grateful for the help of Rafal Skolasinski, who has always been willing to help with the Kwant code, and who has always been patient when answering my questions. I also want to show my thankfulness to Jos Thijssen, who on short notice has offered his time to read my thesis and be the second corrector during my presentation.

CONTENTS

1	PRELIMINARIES	1
1.1	Introduction	1
1.2	Theory of Landau Quantization	2
2	COMPUTATIONAL METHOD	6
2.1	Overview of the Method	6
2.2	Internal truncation theorem	9
3	TESTING ON A TOY MODEL	13
3.1	Toy model definition	13
3.2	Derivation of the analytical solution	15
3.3	Testing the method in two dimensions	17
3.4	Testing the method in three dimensions	18
3.5	Application to the $k \cdot p$ Hamiltonian	19
4	SIMULATION RESULTS	21
4.1	Landau Fans in the trivial and inverted regimes	21
4.2	Magnetic oscillations in the trivial regime	23
4.3	Possibilities for improvement and further research	26
5	CONCLUSION	28
A	THE KDOTP HAMILTONIAN	29
	BIBLIOGRAPHY	30

LIST OF FIGURES

Figure 1	Color mapped plot of the simulated toy model Hamiltonian. 17	
Figure 2	Errors for toy model simulations of 20 and 80 LLs. 18	
Figure 3	Comparison of the analytical and numerical Landau fans for the two-dimensional and three-dimensional toy models. 19	
Figure 4	Plot of the first four LL subblocks of the first row of a simulated $k \cdot p$ Hamiltonian. 20	
Figure 5	Landau fan diagram of the GaSb/InAs/AlSb heterostructure, simulated in the trivial regime. 22	
Figure 6	Simulated dispersion diagrams for the trivial and inverted regimes. 23	
Figure 7	Landau fan diagram of the GaSb/InAs/AlSb heterostructure, simulated in the inverted regime. 24	
Figure 8	Magnetic oscillations in the DOS near the Fermi energy for two broadenings. 25	
Figure 9	FFTs in arbitrary units of the magnetic oscillations in $1/B$, for a range of carrier concentrations and two different broadenings. 26	

ACRONYMS

BGQW	Broken gap quantum well
DOS	Density of states
LL	Landau level
SdH	Shubnikov-de Haas
2DTI	Two-dimensional topological insulator
SOC	Spin orbit coupling
FFT	Fast Fourier transform

PRELIMINARIES

1.1 INTRODUCTION

Two dimensional electron gas (2DEG) systems are an important research subject for future device applications, with possible applications in quantum computing and spintronics. [2, 5, 10, 20]. Particularly interesting are 2DEGs with strong spin orbit coupling (SOC), because their spin properties can be electrically controlled [5, 19].

To research the transport properties of charge carriers in these quantum heterostructures we can study the Fermi surface of the material [1]. A method to experimentally analyze the Fermi surface is placing the material in a changing external magnetic field, and then measuring oscillations in the conductivity. These are called Shubnikov-de Haas (SdH) oscillations. In a simulation we can approximate the SdH oscillations by calculating oscillations in the density of states (DOS) near the Fermi energy. [13, 21, 23]. From the frequency spectrum of the oscillations, one can calculate the extremal cross sections of the Fermi surface perpendicular to the magnetic field [3]. Furthermore, magnetic oscillations are often used to experimentally confirm zero magnetic field spin splitting [5].

In this thesis we develop a computational method that can efficiently simulate Landau levels (LLs) and magnetic oscillations in the DOS. This is a useful tool, for theoretical as well as experimental research. The method is designed to complement Kwant, an open source Python package for numerical calculations on tight-binding models [7]. By using ladder operators, the method inherently uses Landau quantization, which is responsible for the magnetic oscillations. By only using the ladder operators that map between different energy states, we prevent calculating a massive degeneracy in the LLs. In this way we reduce the dimensionality of the problem by one.

We then use this method to simulate GaSb/InAs/AlSb broken gap quantum wells (BGQWs) using an 8×8 Kane Hamiltonian in the standard semiconductor $k \cdot p$ model [17]. We obtain sparse and truncated Hamiltonian matrices for a range of magnetic field strengths, which are then diagonalized to get a Landau fan diagram. From this we calculate the oscillations in the DOS. We then apply a fast Fourier transform (FFT) to analyze the frequency spectrum of these oscillations.

The GaSb/InAs/AlSb materials are regarded as a promising candidate for future device applications [5, 10, 16, 19]. They have high structural compatibility for epitaxial growth due to their approximate

lattice matching, with lattice constants near 0.61 nm [11, 22]. Furthermore, heterostructures of GaSb and InAs are of the broken gap (III) type, meaning that the electrons and holes are confined in the InAs and GaSb layers respectively [8]. We refer to this as hybridization.

The focus of this thesis is on the trivial regime where the electron and hole bands are separated. However, we will also do a simulation of the inverted regime where these bands overlap. This gives rise to a two-dimensional topological insulator (2DTI) phase [16, 19, 22]. This could have applications in topological quantum computing [15, 18]. An advantage of GaSb/InAs compared to other 2DTI's is that the electron and hole bands can be shifted relative to each other by changing the magnetic and electric fields, allowing for a controlled transition between the topological and trivial regimes [9, 19].

In Section 1.2 we review the theory of Landau quantization, which is essential to the rest of the thesis. Derivations of formulas are shown in detail. In Chapter 2, we present the computational method and derive all expressions that are necessary for the method. Furthermore, we prove a theorem that is internally used in the code. In Chapter 3, the developed computational framework is tested with a toy model that can be solved analytically. The toy model takes the Rashba effect as well as the Zeeman effect into account. In Chapter 4, the computational method is applied to calculate the LLs and magnetic oscillations in the DOS of a GaSb/InAs/AlSb BGQW and we discuss the results. Finally, Chapter 5 constitutes the conclusion of the thesis.

1.2 THEORY OF LANDAU QUANTIZATION

In this section we present no new theory, but we give a concise overview of the theory of Landau quantization, that is essential to this thesis. The definitions and also the ladder operators that are being worked towards were obtained from Winkler [23]. The last step in finding the ladder operators uses the same method as Griffiths uses to find them for a harmonic oscillator [6]. If you are already familiar with the theory, you can safely skip to section 2.

The system that we are considering is an electron moving in a two-dimensional plane, extending infinitely far in the x- and y-directions. There is a homogeneous magnetic field perpendicular to the plane of motion:

$$\vec{B} = (0, 0, B). \quad (1)$$

We use the symmetric gauge for the magnetic field [23]:

$$\vec{A}(x, y) = \frac{B}{2}(-y, x, 0). \quad (2)$$

In the presence of a magnetic field, the set of momentum operators is

$$\vec{P} = -i\hbar\nabla + e\vec{A}. \quad (3)$$

We denote $\psi(x, y)$ as ψ and the x- and y-derivative operators as ∂_x and ∂_y . Now we derive the commutation relation for P_x and P_y :

$$\begin{aligned} [P_x, P_y]\psi = & -\hbar^2 \partial_x \partial_y \psi - ie\hbar \frac{B}{2} \partial_x x \psi + ie\hbar \frac{B}{2} y \partial_y \psi - \left(e\frac{B}{2}\right)^2 yx\psi \\ & + \hbar^2 \partial_y \partial_x \psi - ie\hbar \frac{B}{2} \partial_y y \psi + ie\hbar \frac{B}{2} x \partial_x \psi - \left(e\frac{B}{2}\right)^2 xy\psi. \end{aligned} \quad (4)$$

We then cancel some terms:

$$[P_x, P_y]\psi = -ie\hbar \frac{B}{2} \partial_x x \psi + ie\hbar \frac{B}{2} y \partial_y \psi - ie\hbar \frac{B}{2} \partial_y y \psi + ie\hbar \frac{B}{2} x \partial_x \psi \quad . \quad (5)$$

Now we use the product rule, and cancel more terms:

$$\begin{aligned} [P_x, P_y]\psi = & -ie\hbar \frac{B}{2} (\psi + x \partial_x \psi) + ie\hbar \frac{B}{2} y \partial_y \psi \\ & - ie\hbar \frac{B}{2} (\psi + y \partial_y \psi) - ie\hbar \frac{B}{2} x \partial_x \psi \\ = & -ie\hbar B \psi. \end{aligned} \quad (6)$$

Finally, we conclude that

$$[P_x, P_y] = -ie\hbar B. \quad (7)$$

In Eq.(7) we see that because of the presence of a magnetic field, the momenta in different directions do not commute. We notice that the commutator on the right hand side of Eq.(7) is the commutator of the canonical commutation relation $[P_x, x]$ multiplied with a scalar factor of eB . The electron's Hamiltonian is

$$H_L = \frac{1}{2m} (P_x^2 + P_y^2), \quad (8)$$

which shows that the problem has the same algebra as a one-dimensional harmonic oscillator,

$$H_{HO} = \frac{1}{2m} (P_x^2 + (m\omega x)^2). \quad (9)$$

Because of this, we know that ladder operators can be defined that are similar to those of the one-dimensional harmonic oscillator. Because it is the same problem as a harmonic oscillator, we know that the ladder operators will be in agreement with the expression

$$\begin{aligned} H_L = & \frac{1}{2m} (P_x^2 + P_y^2) \\ = & \hbar\omega_c \left(a^\dagger a + \frac{1}{2} \right), \end{aligned} \quad (10)$$

where the cyclotron frequency is [23]

$$\omega_c = \frac{eB}{m}. \quad (11)$$

In a similar way as Griffiths treats the harmonic oscillator [6], we notice that since

$$P_x^2 + P_y^2 = (P_x + iP_y)(P_x - iP_y) + i[P_x, P_y], \quad (12)$$

it is fruitful to look for ladder operators of the form

$$a^\dagger = \beta (P_x + iP_y), \quad a = \beta (P_x - iP_y), \quad (13)$$

where β is a scalar. We then work this out to find the creation and annihilation operators, a^\dagger and a :

$$\begin{aligned} a^\dagger a &= \beta^2 (P_x^2 - iP_x P_y + iP_y P_x + P_y^2) \\ &= \beta^2 (P_x^2 + P_y^2 - i[P_x, P_y]). \end{aligned} \quad (14)$$

Using the commutation relation in Eq.(7) we then express the Hamiltonian in terms of these operators:

$$\begin{aligned} H_L &= \frac{1}{2m} (P_x^2 + P_y^2) \\ &= \frac{1}{2m} \left(\frac{a^\dagger a}{\beta^2} + i[P_x, P_y] \right) \\ &= \hbar\omega_c \left(\frac{a^\dagger a}{\hbar 2eB\beta^2} + \frac{1}{2} \right) \\ &= \hbar\omega_c \left(a^\dagger a + \frac{1}{2} \right). \end{aligned} \quad (15)$$

From this we obtain the same creation and annihilation operators as those that are defined in Winkler [23]:

$$a^\dagger = \frac{1}{\sqrt{2e\hbar B}} (P_x + iP_y), \quad a = \frac{1}{\sqrt{2e\hbar B}} (P_x - iP_y). \quad (16)$$

In a similar way in which we derived Eq.(7), we can show that [23]

$$[a, a^\dagger] = 1. \quad (17)$$

We know from the time-independent Schrödinger equation that

$$H_L \psi = E \psi, \quad (18)$$

where E is the energy eigenvalue of the state vector ψ . We now proof that

$$H_L a^\dagger \psi = (E + \hbar\omega_c) a^\dagger \psi. \quad (19)$$

First we act the Hamiltonian on $a^\dagger \psi$:

$$\begin{aligned} H_L a^\dagger \psi &= \hbar\omega_c \left(a^\dagger a + \frac{1}{2} \right) a^\dagger \psi \\ &= \hbar\omega_c \left(a^\dagger a a^\dagger + \frac{1}{2} a^\dagger \right) \psi \\ &= \hbar\omega_c a^\dagger \left(a a^\dagger + \frac{1}{2} \right) \psi. \end{aligned} \quad (20)$$

Now we use the commutation relation in Eq.(17):

$$\begin{aligned}
 H_L a^\dagger \psi &= \hbar\omega_c a^\dagger \left(1 + a^\dagger a + \frac{1}{2} \right) \psi \\
 &= \hbar\omega_c a^\dagger \left(a^\dagger a + \frac{3}{2} \right) \psi \\
 &= a^\dagger (H_L + \hbar\omega_c) \psi \\
 &= a^\dagger (E + \hbar\omega_c) \psi \\
 &= (E + \hbar\omega_c) a^\dagger \psi.
 \end{aligned} \tag{21}$$

From this we can conclude that a^\dagger is a raising operator. One can follow the same procedure to show that a is a lowering operator. The energy eigenvalues of the system are

$$\begin{aligned}
 E_n &= \hbar\omega_c \langle N | a^\dagger a | N \rangle + \hbar\omega_c \langle N | \frac{1}{2} | N \rangle \\
 &= \hbar\omega_c \langle N | a^\dagger \sqrt{N} | N-1 \rangle + \hbar\omega_c \frac{1}{2} \\
 &= \hbar\omega_c \langle N | \sqrt{N} \sqrt{N} | N \rangle + \hbar\omega_c \frac{1}{2} \\
 &= \hbar\omega_c \left(N + \frac{1}{2} \right).
 \end{aligned} \tag{22}$$

From this last expression we see that the energy eigenvalues of the system are quantized into LLs. Because ω_c scales linearly with B , the differences between the energy levels will also scale linearly with B . We remark that because there are two dimensions there is also another set of ladder operators b^\dagger and b [23]:

$$b^\dagger = \frac{1}{\sqrt{2e\hbar B}} (P_x^- - iP_y^-), \quad b = \frac{1}{\sqrt{2e\hbar B}} (P_x^- + iP_y^-), \tag{23}$$

where

$$\vec{P}^- = -i\hbar\nabla - e\vec{A}. \tag{24}$$

These ladder operators map between different states with the same energy. The quantum numbers $a^\dagger a$, $b^\dagger b$, and the substructure of the $k \cdot p$ Hamiltonian make the basis complete. We leave the $b^\dagger b$ substructure out of the Hamiltonian, because we are interested in the different energy levels, and by doing this we reduce the dimensionality of the problem by one.

COMPUTATIONAL METHOD

In this chapter we look at the computational framework that can simulate LLs. It is specifically designed to be used with heterostructure systems where there is an external homogeneous magnetic field in the growth direction of the layers. We apply the framework to a GaSb/InAs/AlSb heterostructure, but the framework is universal and can also be used to research other materials. In the first section the computational method is discussed and we derive all necessary expressions. In the second section there is a proof of a truncation theorem that is internally used in the code of the computational method. The code was written in Python, but this chapter is written in a general way, and knowledge of Python is not required to read it. The relevant Python modules are mentioned, but these can be ignored if desired.

2.1 OVERVIEW OF THE METHOD

The key principle of the computational method is that we can express the momentum operators in terms of the creation and annihilation operators. We do this by addition or subtraction of Eqs.(16), resulting in the following expressions:

$$P_x = \sqrt{\frac{\hbar e B}{2}} (a^\dagger + a), \quad P_y = \sqrt{\frac{\hbar e B}{2}} (a - a^\dagger) i. \quad (25)$$

We exploit this by expressing the ladder operators in matrix form in the basis of the LL eigenstates. These are infinitely sized matrices with one nonzero diagonal that follows a certain pattern. To see this, we first define the infinitely dimensional basis of LL eigenstates

$$\mathcal{L} = \{|N=0\rangle, |N=1\rangle, |N=2\rangle, \dots\}, \quad (26)$$

which will be referred to as the LL basis. The goal now is to express the ladder operators within this basis. Now we notice that

$$\langle N | a^\dagger | N' \rangle = 0, \quad \text{if } N \neq N' + 1. \quad (27)$$

This is because the creation operator raises the Landau number of the ket by one. Because the different Landau number states are mutually orthogonal, this means that if the Landau number in the bra is not one higher than the Landau number in the ket, the inner product will always be zero. We also see that

$$\text{when } N = N' + 1, \quad (28)$$

we get the equation

$$\begin{aligned}\langle N' + 1 | a^\dagger | N' \rangle &= \langle N' + 1 | \sqrt{N' + 1} | N' + 1 \rangle \\ &= \sqrt{N' + 1}.\end{aligned}\quad (29)$$

Now we can make a compact general expression for a^\dagger in the \mathcal{L} basis using the kronecker delta:

$$(a_{\mathcal{L}}^\dagger)_{i,j} = \delta_{i,j+1} \sqrt{j}, \quad (30)$$

where $a_{\mathcal{L},ij}^\dagger$ is matrix element i, j of the operator in the \mathcal{L} basis. With the same arguments, we find an expression for the operator a in the \mathcal{L} basis:

$$(a_{\mathcal{L}})_{i,j} = \delta_{i,j-1} \sqrt{i}. \quad (31)$$

Here we could also have used the Hermitian conjugate property of the ladder operators. In the Python code we can define truncated versions of these matrices as finite square NumPy arrays.

The eigenvalues of the truncated Hamiltonian are an approximation of the eigenvalues of the real and infinitely sized Hamiltonian, because there is coupling between different LLs. In Section 3.3 we test the method on an analytically solvable toy model Hamiltonian, and we demonstrate the effect of the coupling and approximation. For a qualitative discussion of the effects of the approximation on the $k \cdot p$ Hamiltonian, see Section 3.5.

By first truncating the ladder operators, and then forming momentum operators by taking products of these ladder operators, we would be making an extra approximation if we would not account for this. If we want N LLs, we overcome this problem by truncating the ladder operators to $N + \frac{M}{2}$. Here M is the maximum power of the momentum operator products. If M is an odd number, we round up. In Section 2.2 we prove that by doing this our approximation is equivalent to truncation of the Hamiltonian.

What is also important for our computational method is that we separate the Hamiltonian in groups of momentum operators. This concept can most easily be explained with a demonstration. We first demonstrate this for a two-dimensional Hamiltonian, and afterwards we will show how we use Kwant to solve the problem in the z -direction. Consider the following example Hamiltonian:

$$H_S = \frac{1}{2m} (P_x^2 + P_y^2) I_2 + \frac{g_n}{2} \mu_B B \sigma_z + \alpha (\sigma_x P_y - \sigma_y P_x), \quad (32)$$

where I_2 is the 2×2 identity matrix and $\zeta(z)$ is a z -dependent variable. This Hamiltonian can also be expressed as:

$$\begin{aligned}H_S &= P_x^2 \begin{pmatrix} \frac{1}{2m} & 0 \\ 0 & \frac{1}{2m} \end{pmatrix} + P_y^2 \begin{pmatrix} \frac{1}{2m} & 0 \\ 0 & \frac{1}{2m} \end{pmatrix} + P_x \begin{pmatrix} 0 & \alpha \\ \alpha & 0 \end{pmatrix} \\ &+ P_y \begin{pmatrix} 0 & i\alpha \\ -i\alpha & 0 \end{pmatrix} + 1 \begin{pmatrix} \frac{g_n}{2} \mu_B B & 0 \\ 0 & -\frac{g_n}{2} \mu_B B \end{pmatrix}.\end{aligned}$$

In the code we can enter Eq.(32) as a Sympy expression. The code that was written for this thesis then makes these pairs:

$$\left\{ P_x^2 : \begin{pmatrix} \frac{1}{2m} & 0 \\ 0 & \frac{1}{2m} \end{pmatrix}, P_y^2 : \begin{pmatrix} \frac{1}{2m} & 0 \\ 0 & \frac{1}{2m} \end{pmatrix}, P_x : \begin{pmatrix} 0 & \alpha \\ \alpha & 0 \end{pmatrix}, \right. \\ \left. P_y : \begin{pmatrix} 0 & i\alpha \\ -i\alpha & 0 \end{pmatrix}, 1 : \begin{pmatrix} \frac{g_n}{2}\mu_B B & 0 \\ 0 & -\frac{g_n}{2}\mu_B B \end{pmatrix} \right\}. \quad (33)$$

The reader who is familiar with Python will recognise a Python dictionary in this structure. The final Hamiltonian can be formed by taking the sum of the Kronecker products of these pairs Hamiltonians. As an example we now show, first only for the P_x^2 term, how this is done when using three LLs. After that we will explain how we use Kwant to simulate in the z-dimension. Because there is a power of two and we want to simulate three LLs, we first truncate the ladder operators to the 4×4 matrices

$$a_4^\dagger = \begin{pmatrix} 0 & 0 & 0 & 0 \\ 1 & 0 & 0 & 0 \\ 0 & \sqrt{2} & 0 & 0 \\ 0 & 0 & \sqrt{3} & 0 \end{pmatrix}, \quad a_4 = \begin{pmatrix} 0 & 1 & 0 & 0 \\ 0 & 0 & \sqrt{2} & 0 \\ 0 & 0 & 0 & \sqrt{3} \\ 0 & 0 & 0 & 0 \end{pmatrix}. \quad (34)$$

Here we must remark that in the computation we use numerical matrices. We then use Eq.(25) to calculate the matrix

$$\frac{\hbar e B}{2} (a_4^\dagger + a_4)^2 = \frac{\hbar e B}{2} \begin{pmatrix} 1 & 0 & \sqrt{2} & 0 \\ 0 & 3 & 0 & \sqrt{6} \\ \sqrt{2} & 0 & 5 & 0 \\ 0 & \sqrt{6} & 0 & 3 \end{pmatrix}. \quad (35)$$

Then we truncate this matrix to

$$(P_x^2)_3 = \frac{\hbar e B}{2} \begin{pmatrix} 1 & 0 & \sqrt{2} \\ 0 & 3 & 0 \\ \sqrt{2} & 0 & 5 \end{pmatrix}. \quad (36)$$

We then take the Kronecker product to get the 6×6 matrix

$$(P_x^2)_3 \otimes \begin{pmatrix} \frac{1}{2m} & 0 \\ 0 & \frac{1}{2m} \end{pmatrix} = \frac{\hbar e B}{4m} \begin{pmatrix} 1 & 0 & 0 & 0 & \sqrt{2} & 0 \\ 0 & 1 & 0 & 0 & 0 & \sqrt{2} \\ 0 & 0 & 3 & 0 & 0 & 0 \\ 0 & 0 & 0 & 3 & 0 & 0 \\ \sqrt{2} & 0 & 0 & 0 & 5 & 0 \\ 0 & \sqrt{2} & 0 & 0 & 0 & 5 \end{pmatrix}. \quad (37)$$

These steps are performed for all the pairs in Eq.(33). Finally, we then take the sum of these pairs to get the total Hamiltonian.

We are simulating a three-dimensional system, so there are also P_z momentum operators, or powers thereof, and possibly z -dependent variables. We now illustrate how we then combine the ladder operator method with Kwant to solve the three dimensional problem. For example, for a three dimensional Hamiltonian, in the group of pairs in Eq.33 there could also have been the following pair:

$$\left\{ P_x^2 : \begin{pmatrix} \frac{P_z^2}{2m} + \zeta(z) & 0 \\ 0 & \frac{P_z^2}{2m} + \zeta(z) \end{pmatrix} \right\}. \quad (38)$$

In this example there would be a product in the Hamiltonian of P_x^2 with a P_z^2 momentum operators plus a z -dependent variable $\zeta(z)$. The Hamiltonian of the matrix on the right hand side of the colon is calculated using Kwant. We can then perform the step in Eq.(37) with the Hamiltonian from Kwant. The final result of the addition of all these pairs is a sparse Hamiltonian matrix. We then use sparse matrix diagonalization to find a specified amount of energy eigenvalues.

2.2 INTERNAL TRUNCATION THEOREM

In the LL basis \mathcal{L} , a projector P_n that projects the quantum state vector on the n lowest LLs, can be defined as:

$$(P_n)_{i,j} = \begin{cases} \delta_{i,j}, & \text{if } i \leq n \text{ and } j \leq n \\ 0, & \text{otherwise.} \end{cases} \quad (39)$$

Let us define two variables k and l as $k, l \in \mathbb{N}$. We can reason that when P_k acts on a square matrix M from the left, all entries with row index greater than k become zero. Likewise, when P_l acts on M from the right, all entries with column index greater than l become zero:

$$(P_k M)_{i,j} = \begin{cases} (M)_{i,j}, & \text{if } i \leq k \\ 0, & \text{otherwise,} \end{cases} \quad (40)$$

$$(M P_l)_{i,j} = \begin{cases} (M)_{i,j}, & \text{if } j \leq l \\ 0, & \text{otherwise.} \end{cases} \quad (41)$$

By using the same reasoning, or by combining Eq.(40) and Eq.(41), we see that

$$(P_k M P_l)_{i,j} = \begin{cases} (M)_{i,j}, & \text{if } i \leq k \text{ and } j \leq l \\ 0, & \text{otherwise.} \end{cases} \quad (42)$$

Now this result is applied to a^\dagger , which we obtained in Eq.(30). For a^\dagger this results in

$$(P_k a^\dagger)_{i,j} = \begin{cases} \delta_{i,j+1} \sqrt{j}, & \text{if } i \leq k \\ 0, & \text{otherwise,} \end{cases} \quad (43)$$

$$(P_k a^\dagger P_l)_{i,j} = \begin{cases} \delta_{i,j+1} \sqrt{j}, & \text{if } i \leq k \text{ and } j \leq l \\ 0, & \text{otherwise.} \end{cases} \quad (44)$$

This set of equations is equal to

$$(P_k a^\dagger)_{i,j} = \begin{cases} \sqrt{j}, & \text{if } i \leq k \text{ and } i = j + 1 \\ 0, & \text{otherwise,} \end{cases} \quad (45)$$

$$(P_k a^\dagger P_l)_{i,j} = \begin{cases} \sqrt{j}, & \text{if } i \leq k \text{ and } j \leq l \text{ and } i = j + 1 \\ 0, & \text{otherwise.} \end{cases} \quad (46)$$

Now we can see that in the case $l > k$, the conditional statements of Eq.(45) and Eq.(46) are equal:

$$\begin{aligned} & (\text{if } i \leq k \text{ and } i = j + 1) \\ & = (\text{if } j + 1 \leq k), \end{aligned} \quad (47)$$

$$\begin{aligned} & (\text{if } i \leq k \text{ and } j \leq l \text{ and } i = j + 1) \\ & = (\text{if } j + 1 \leq k \text{ and } j \leq l) \\ & = (\text{if } j + 1 \leq k), \quad \text{if } l > k. \end{aligned} \quad (48)$$

From this it follows that

$$P_k a^\dagger = P_k a^\dagger P_l, \quad \text{if } l > k. \quad (49)$$

In the same way, we can show that

$$a^\dagger P_k = P_l a^\dagger P_k, \quad \text{if } l > k. \quad (50)$$

By taking the Hermitian conjugate of these expressions we see that the same holds for a . This results in the following two lemmas:

$$\begin{aligned} P_k a^{(+)} &= P_k a^{(+)} P_l, \quad \text{if } l > k \\ a^{(+)} P_k &= P_l a^{(+)} P_k, \quad \text{if } l > k, \end{aligned} \quad (51)$$

where $a^{(+)}$ denotes either a or a^\dagger , with the same operator on both sides of the equation. From Eqs.(25) we see that a product of m momentum operators can be expressed as:

$$M = \prod_{i=1}^m (\alpha_i a + \beta_i a^\dagger). \quad (52)$$

To shorten notation we define the symbol

$$\Pi \equiv P_n \prod_{i=1}^m \left(P_{n+\frac{m}{2}} \left(\alpha_i a + \beta_i a^\dagger \right) P_{n+\frac{m}{2}} \right) P_n. \quad (53)$$

Now we state that truncating the momentum operators to $n + \frac{m}{2} \times n + \frac{m}{2}$ and then truncating the product of these truncated operators to $n \times n$, is equal to truncating the infinitely sized matrix M to $n \times n$. To prove this statement, we need to prove that

$$\Pi = P_n M P_n. \quad (54)$$

We can expand $P_n M P_n$ to get

$$\begin{aligned} P_n M P_n &= P_n (\alpha_0 a^\dagger + \beta_0 a) (\alpha_1 a^\dagger + \beta_1 a) \cdot (\cdots) \\ &\quad \cdot (\alpha_{\frac{m}{2}} a^\dagger + \beta_{\frac{m}{2}} a) \cdot (\cdots) \\ &\quad \cdot (\alpha_{m-1} a^\dagger + \beta_{m-1} a) (\alpha_m a^\dagger + \beta_m a) P_n. \end{aligned} \quad (55)$$

Using the first lemma in Eq.(51), we can write this as

$$\begin{aligned} P_n M P_n &= P_n (\alpha_0 a^\dagger + \beta_0 a) P_{n+1} (\alpha_1 a^\dagger + \beta_1 a) P_{n+2} (\cdots) \\ &\quad \cdot P_{n+\frac{m}{2}} (\alpha_{\frac{m}{2}} a^\dagger + \beta_{\frac{m}{2}} a) \cdot (\cdots) \\ &\quad \cdot (\alpha_{m-1} a^\dagger + \beta_{m-1} a) (\alpha_m a^\dagger + \beta_m a) P_n. \end{aligned} \quad (56)$$

Now we use the second lemma in Eq.(51) to arrive at

$$\begin{aligned} P_n M P_n &= P_n (\alpha_0 a^\dagger + \beta_0 a) P_{n+1} (\alpha_1 a^\dagger + \beta_1 a) P_{n+2} (\cdots) \\ &\quad \cdot P_{n+\frac{m}{2}} (\alpha_{\frac{m}{2}} a^\dagger + \beta_{\frac{m}{2}} a) P_{n+\frac{m}{2}} \cdot (\cdots) \\ &\quad \cdot P_{n+2} (\alpha_{m-1} a^\dagger + \beta_{m-1} a) P_{n+1} (\alpha_m a^\dagger + \beta_m a) P_n. \end{aligned} \quad (57)$$

We expand Π to get the equation:

$$\begin{aligned} \Pi &= P_n P_{n+\frac{m}{2}} (\alpha_0 a^\dagger + \beta_0 a) P_{n+\frac{m}{2}}^2 (\alpha_1 a^\dagger + \beta_1 a) P_{n+\frac{m}{2}}^2 (\cdots) \\ &\quad \cdot P_{n+\frac{m}{2}}^2 (\alpha_{\frac{m}{2}} a^\dagger + \beta_{\frac{m}{2}} a) P_{n+\frac{m}{2}}^2 \cdot (\cdots) \\ &\quad \cdot P_{n+\frac{m}{2}}^2 (\alpha_{m-1} a^\dagger + \beta_{m-1} a) P_{n+\frac{m}{2}}^2 (\alpha_m a^\dagger + \beta_m a) P_{n+\frac{m}{2}} P_n. \\ &= P_n (\alpha_0 a^\dagger + \beta_0 a) P_{n+\frac{m}{2}} (\alpha_1 a^\dagger + \beta_1 a) P_{n+\frac{m}{2}} (\cdots) \\ &\quad \cdot P_{n+\frac{m}{2}} (\alpha_{\frac{m}{2}} a^\dagger + \beta_{\frac{m}{2}} a) P_{n+\frac{m}{2}} \cdot (\cdots) \\ &\quad \cdot P_{n+\frac{m}{2}} (\alpha_{m-1} a^\dagger + \beta_{m-1} a) P_{n+\frac{m}{2}} (\alpha_m a^\dagger + \beta_m a) P_n. \end{aligned} \quad (58)$$

Now we use the two lemmas in Eq.(51) to write this as

$$\begin{aligned} \Pi &= P_n (\alpha_0 a^\dagger + \beta_0 a) P_{n+1} P_{n+\frac{m}{2}} (\alpha_1 a^\dagger + \beta_1 a) P_{n+\frac{m}{2}} (\cdots) \\ &\quad \cdot P_{n+\frac{m}{2}} (\alpha_{\frac{m}{2}} a^\dagger + \beta_{\frac{m}{2}} a) P_{n+\frac{m}{2}} \cdot (\cdots) \\ &\quad \cdot P_{n+\frac{m}{2}} (\alpha_{m-1} a^\dagger + \beta_{m-1} a) P_{n+\frac{m}{2}} P_{n+1} (\alpha_m a^\dagger + \beta_m a) P_n. \\ &= P_n (\alpha_0 a^\dagger + \beta_0 a) P_{n+1} (\alpha_1 a^\dagger + \beta_1 a) P_{n+2} P_{n+\frac{m}{2}} (\cdots) \\ &\quad \cdot P_{n+\frac{m}{2}} (\alpha_{\frac{m}{2}} a^\dagger + \beta_{\frac{m}{2}} a) P_{n+\frac{m}{2}} \cdot (\cdots) \\ &\quad \cdot P_{n+\frac{m}{2}} P_{n+2} (\alpha_{m-1} a^\dagger + \beta_{m-1} a) P_{n+1} (\alpha_m a^\dagger + \beta_m a) P_n. \end{aligned} \quad (59)$$

This step can be iterated to arrive at

$$\begin{aligned}
 \Pi &= P_n(\alpha_0 a^\dagger + \beta_0 a) P_{n+1}(\alpha_1 a^\dagger + \beta_1 a) P_{n+2}(\cdots) \\
 &\quad \cdot P_{n+\frac{m}{2}}(\alpha_{\frac{m}{2}} a^\dagger + \beta_{\frac{m}{2}} a) P_{n+\frac{m}{2}} \cdot (\cdots) \\
 &\quad \cdot P_{n+2}(\alpha_{m-1} a^\dagger + \beta_{m-1} a) P_{n+1}(\alpha_m a^\dagger + \beta_m a) P_n.
 \end{aligned} \tag{60}$$

We can now see that Eqs. (57) and (60) are the same:

$$\Pi = P_n M P_n. \tag{61}$$

TESTING ON A TOY MODEL

We test the computational method on an analytically solvable toy model Hamiltonian that includes the Zeeman and Rashba effects. We include the Rashba effect because GaSb/InAs heterostructures exhibit strong SOC. The Rashba effect, caused by structural inversion asymmetry (SIA) dominates the Dresselhaus effect, which is due to bulk inversion asymmetry (BIA). [5, 14]. We perform a simulation on this toy model, and then compare the results with the analytic solutions. We first do this in two dimensions, and then in three dimensions. The particle is confined to a few nanometers in the third dimension.

The test of the two-dimensional model relies only on the code that was written for this thesis, and not on Kwant. The purpose of this test is to see whether the simulation behaves as expected. That is, if the errors occur where they are expected and if the other solutions are correct to sufficient precision.

For the three-dimensional model we are testing whether Kwant is combined correctly with this code, it is not our purpose to test Kwant itself. Because the Schrödinger equation in the third dimension is separable from the two other dimensions, the Landau fan diagram of the three-dimensional model will consist of shifted copies of the fan of the two-dimensional model. Because of this the implementation can simply be checked by computing these energy shifts with Kwant, and then using these to shift the fan that was calculated for the two-dimensional model. This should then deliver the same result as performing a simulation on the three-dimensional model.

Before we test the method, we first do some necessary derivations. From Winkler[23] we see that the toy model Hamiltonian can be expressed in terms of the ladder operators that are defined in (16). We show why this Hamiltonian can be expressed in this form, starting with the Rashba Hamiltonian in the form in which it was originally defined by Rashba and Bychkov. Winkler also provides us with an analytical solution to the toy model Hamiltonian, of which we work out a detailed derivation.

3.1 TOY MODEL DEFINITION

First, we define the Pauli matrices:

$$\sigma_x = \begin{pmatrix} 0 & 1 \\ 1 & 0 \end{pmatrix}, \quad \sigma_y = \begin{pmatrix} 0 & -i \\ i & 0 \end{pmatrix}, \quad \sigma_z = \begin{pmatrix} 1 & 0 \\ 0 & -1 \end{pmatrix}. \quad (62)$$

We also define the Pauli z-basis

$$\mathcal{S} = \left\{ \begin{pmatrix} 1 \\ 0 \end{pmatrix}, \begin{pmatrix} 0 \\ 1 \end{pmatrix} \right\}, \quad (63)$$

where the first state denotes spin pointing in the positive z direction (spin up), and the second one denotes spin pointing in the negative z direction (spin down). The toy model Hamiltonian in the Pauli-z basis is [23]:

$$H_S = \hbar\omega_c \left(a^\dagger a + \frac{1}{2} \right) I_2 + \frac{g_n}{2} \mu_B B \sigma_z + \sqrt{\frac{2eB}{\hbar}} \alpha \begin{pmatrix} 0 & ia \\ -ia^\dagger & 0 \end{pmatrix}. \quad (64)$$

The first part of the Hamiltonian ($H_{L,S}$) represents the Landau quantization, this part is the same as Eq.(10), which we derived in section 1.2. The second part ($H_{Z,S}$) is the Zeeman effect. This is covered in many introductory quantum mechanics textbooks, such as Griffiths [6]. The third part ($H_{R,S}$) is the Rashba effect. The Rashba Hamiltonian is defined by Rashba and Bychkov as [4]:

$$H_{R,S} = \alpha (\vec{\sigma} \times \vec{p}) \cdot \hat{z}. \quad (65)$$

Here $\vec{\sigma}$ is a vector of the Pauli matrices, and \hat{z} is a unit vector in the z direction. The unit vector is perpendicular to the plane of motion, which in our case is the x-y plane. The Rashba Hamiltonian of Eq.(65) is the same as the last part of Eq.(64). To see this we take the cross product and the dot product, and then use Eq.(16) to express it in terms of ladder operators:

$$\begin{aligned} H_{R,S} &= \alpha (\vec{\sigma} \times \vec{p}) \cdot \hat{z} \\ &= \alpha (\sigma_x P_y - \sigma_y P_x) \\ &= \alpha \begin{pmatrix} 0 & P_y + iP_x \\ P_y - iP_x & 0 \end{pmatrix} \\ &= \sqrt{\frac{2eB}{\hbar}} \alpha \begin{pmatrix} 0 & ia \\ -ia^\dagger & 0 \end{pmatrix}. \end{aligned} \quad (66)$$

From Eq.(10) and Eq.(65) we see that we can also express Eq.(64) as

$$H_S = \frac{1}{2m} (P_x^2 + P_y^2) I_2 + \frac{g_n}{2} \mu_B B \sigma_z + \alpha (\sigma_x P_y - \sigma_y P_x). \quad (67)$$

This is the symbolic form in which we put the Hamiltonian into the computational code. The analytic solution to the toy model Hamiltonian is given by Winkler [23]:

$$E_{N\pm} = \hbar\omega_c \left(N + \frac{1}{2} \pm \frac{1}{2} \right) \mp \frac{1}{2} \sqrt{(\hbar\omega_c - g\mu_B B)^2 \pm \frac{8eB}{\hbar} \alpha^2 \left(N + \frac{1}{2} \pm \frac{1}{2} \right)}. \quad (68)$$

Here N denotes the LL and plus and minus denote different spin states. In the following section we derive this solution in detail.

3.2 DERIVATION OF THE ANALYTICAL SOLUTION

First we define a basis that not only contains two spin states, but also two consecutive LLs:

$$\mathcal{B} = \{|N, \uparrow\rangle, |N+1, \downarrow\rangle\}. \quad (69)$$

Where $|N, \uparrow\rangle$ is a state with LL N and spin up, and $|N+1, \downarrow\rangle$ is a state with LL $N+1$ and spin down. We can use this small basis, because there is only coupling between these states. To express the toy model Hamiltonian in this basis, we do the following calculation:

$$\begin{pmatrix} \langle N, \uparrow | H | N, \uparrow \rangle & \langle N, \uparrow | H | N+1, \downarrow \rangle \\ \langle N+1, \downarrow | H | N, \uparrow \rangle & \langle N+1, \downarrow | H | N+1, \downarrow \rangle \end{pmatrix}. \quad (70)$$

This is done separately for the three parts of the Hamiltonian. First the LL part:

$$\begin{aligned} H_{L,\mathcal{B}} &= \hbar\omega_c \begin{pmatrix} N + \frac{1}{2} & 0 \\ 0 & N + \frac{3}{2} \end{pmatrix} \\ &= \hbar\omega_c \left[(N+1)I_2 - \frac{1}{2}\sigma_z \right]. \end{aligned} \quad (71)$$

The Zeeman part of the Hamiltonian in the basis \mathcal{B} is the same as in the basis \mathcal{S} , because this part is independent of the LL N , and the ordering of spin states is the same in both bases:

$$H_{Z,\mathcal{B}} = \frac{g_n}{2} \mu_B B \sigma_z. \quad (72)$$

Now the Rashba part:

$$\begin{aligned} H_{R,\mathcal{B}} &= \sqrt{\frac{2eB}{\hbar}} \alpha \begin{pmatrix} 0 & i\sqrt{N+1} \\ -i\sqrt{N+1} & 0 \end{pmatrix} \\ &= -\sqrt{\frac{2eB}{\hbar}} \alpha \sqrt{N+1} \sigma_y. \end{aligned} \quad (73)$$

From this we find that the toy model Hamiltonian in the basis \mathcal{B} is

$$H_{\mathcal{B}} = \hbar\omega_c (N+1)I_2 - \sqrt{\frac{2eB}{\hbar}} \alpha \sqrt{N+1} \sigma_y + \left(\frac{g_n}{2} \mu_B B - \frac{1}{2} \hbar\omega_c \right) \sigma_z. \quad (74)$$

We first notice that since the Pauli matrices in combination with the identity matrix form a complete basis set for the 2×2 matrices, the Hamiltonian can be expressed as

$$a_I I_2 + a_x \sigma_x + a_y \sigma_y + a_z \sigma_z = \begin{pmatrix} a_I + a_z & a_x - ia_y \\ a_x + ia_y & a_I - a_z \end{pmatrix}. \quad (75)$$

In fact, the Hamiltonian in Eq.(74) is already expressed in this form. To find the eigenvalues of the Hamiltonian, we first show that

$$\lambda_{\pm} = a_I \pm \sqrt{a_x^2 + a_y^2 + a_z^2}, \quad (76)$$

where λ_{\pm} are the two eigenvalues. We see tht this is true when we solve the characteristic polynomial equation

$$\begin{vmatrix} a_I + a_z - \lambda_{\pm} & a_x - ia_y \\ a_x + ia_y & a_I - a_z - \lambda_{\pm} \end{vmatrix} = 0. \quad (77)$$

From this we see that

$$\begin{aligned} (a_I + a_z + \lambda_{\pm})(a_I - a_z - \lambda_{\pm}) - (a_x^2 + a_y^2) &= 0 \\ (a_I - \lambda_{\pm}) &= \pm \sqrt{a_x^2 + a_y^2 + a_z^2} \\ \lambda_{\pm} &= a_I \pm \sqrt{a_x^2 + a_y^2 + a_z^2}. \end{aligned} \quad (78)$$

Applying Eq.(76) to the toy model Hamiltonian in Eq.(74) results in the following equation for the eigenvalues:

$$\lambda_{\pm} = \hbar\omega_c(N+1) \pm \frac{1}{2}\sqrt{(\hbar\omega_c - g_n\mu_B B)^2 + \frac{8eB}{\hbar}\alpha^2(N+1)} \quad (79)$$

These two energy eigenvalues are the eigenvalues for the $|N, \uparrow\rangle$ and $|N+1, \downarrow\rangle$ eigenstates. Because the energy is higher for higher LLs, and because the spin down state has a higher energy than the spin up state, λ_+ must be the eigenvalue for $|N+1, \downarrow\rangle$ and λ_- must be the eigenvalue for $|N, \uparrow\rangle$:

$$E_{N,\uparrow} = \hbar\omega_c(N+1) - \frac{1}{2}\sqrt{(\hbar\omega_c - g_n\mu_B B)^2 + \frac{8eB}{\hbar}\alpha^2(N+1)}. \quad (80)$$

$$E_{N+1,\downarrow} = \hbar\omega_c(N+1) + \frac{1}{2}\sqrt{(\hbar\omega_c - g_n\mu_B B)^2 + \frac{8eB}{\hbar}\alpha^2(N+1)}. \quad (81)$$

By substituting $N+1$ with N in Eq.(81), we find the following equation for the eigenvalues of the state $|N, \downarrow\rangle$:

$$E_{N,\downarrow} = \hbar\omega_c N + \frac{1}{2}\sqrt{(\hbar\omega_c - g_n\mu_B B)^2 + \frac{8eB}{\hbar}\alpha^2 N}. \quad (82)$$

We can then combine Eq.(80) and Eq.(82) into one equation:

$$E_{N\pm} = \hbar\omega_c \left(N + \frac{1}{2} \pm \frac{1}{2} \right) \mp \frac{1}{2}\sqrt{(\hbar\omega_c - g_n\mu_B B)^2 \pm \frac{8eB}{\hbar}\alpha^2 \left(N + \frac{1}{2} \pm \frac{1}{2} \right)}. \quad (83)$$

This is the same solution as Eq.(68), which we obtained from Winkler [23].

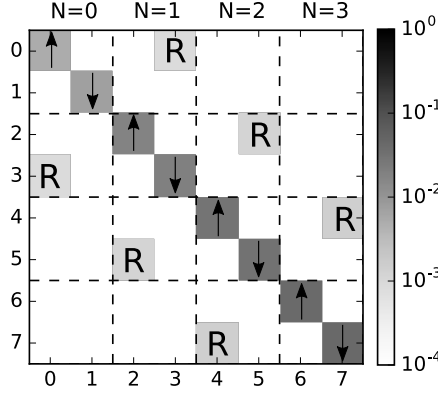


Figure 1: Plot of the two-dimensional toy model Hamiltonian, resulting from a simulation. The LL subblocks are shown with dashes. Spin states are denoted with arrows, and the Rashba coupling elements are labeled with an R. The color map shows the magnitude of the element values. Energies are in eV, however it is the relative magnitude of the elements that is of interest.

3.3 TESTING THE METHOD IN TWO DIMENSIONS

If we look at the toy model Hamiltonian in Eq.(64), we see that the off diagonal element above the diagonal is ia and the off diagonal element below the diagonal is $-ia^\dagger$. This tells us that the state $|N, \uparrow\rangle$ is coupled to $|N+1, \downarrow\rangle$, and $|N, \downarrow\rangle$ is coupled to $|N-1, \uparrow\rangle$. Because of this we expect that if the computational method works correctly, truncation will only result in a significant error for the eigenvalue belonging to $|N, \uparrow\rangle$. This energy level has index $2N-2$, because we are counting from zero and there are two energy eigenvalues per LL.

First we do the simulation for 80 LLs and look at the first 8×8 subblock of the resulting Hamiltonian matrix for a magnetic field strength of 2.5 T. With some added annotations, this results in the plot of Figure 1. In the plot we can see the couplings, and also the increasing energies for higher LLs.

Now we also perform the simulation for 20, 40, and 60 and 80 LLs and check whether there is indeed only a significant error in the energy level with index $2N-2$. In Figure 2 the errors are plotted for 20 and 80 LLs for a magnetic field strength of 2.5 T. From these plots we can see that there only is a significant error at energy level $2N-1$. This error is of order 1 meV. All other errors are of order 10^{-15} eV or lower. This observation holds for magnetic field strengths higher than 1 T. For lower B values there is a second significant error, of order 0.1 meV. This error is in one of the topmost LLs.

In figure 9a we show the Landau fan diagram of the simulation results for magnetic field strengths in a range from 0 to 5 T. Here the analytical results are plotted as blue lines, and the numerical results are plotted with dashes. The white part in the top left area of the fig-

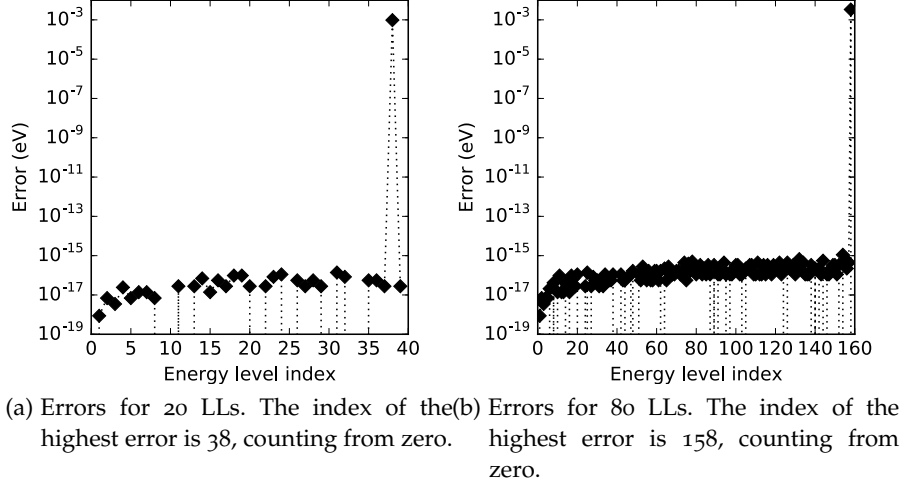


Figure 2: Errors for simulations of 20 and 80 LLs, with a magnetic field strength of 2.5 T

ure comes from the truncation. The empty area is where the missing LLs for $N > 80$ would be if there was no truncation. The spin splitting is clearly visible for large B . We see that the numerical and analytic fans nicely overlap. The computational method in two dimensions behaves as expected, the only significant errors are in the topmost LLs.

3.4 TESTING THE METHOD IN THREE DIMENSIONS

In order to do the computation in three dimensions, we need to extend the toy model Hamiltonian to be three dimensional. To do this, we extend Eq.(67) to

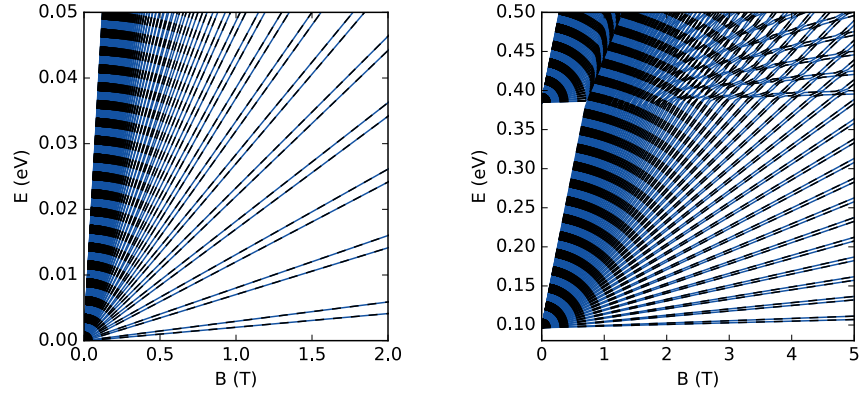
$$H_S = \frac{1}{2m} (P_x^2 + P_y^2 + P_z^2) I_2 + \frac{g_n}{2} \mu_B B \sigma_z + \alpha (\sigma_x P_y - \sigma_y P_x). \quad (84)$$

Here we have simply added the z-direction free particle Hamiltonian to the original Hamiltonian. Since the z-direction Hamiltonian is separable from the Hamiltonian in the x- and y-directions, the Landau fan diagram of the three-dimensional toy model will consist of shifted copies of the two-dimensional model's Landau fan. The energy shifts will be the energy eigenvalues of

$$H_Z = \frac{P_z^2}{2m}. \quad (85)$$

Here we are taking into account that we are dealing with a system with a finite dimension in the z-direction. Kwant uses a tight-binding model, which approximates the free electron model, and we use Kwant to calculate the energy shifts.

To test the implementation of Kwant, we compare two calculations. First, we calculate the energy shifts by simulating Eq.(85) with Kwant.



(a) Landau fans for the two-dimensional toy model. (b) Landau fans for the three-dimensional toy model.

Figure 3: Comparison of the analytical and numerical Landau fans for the two-dimensional and three-dimensional toy models. The analytic solution is plotted as a blue line and the numerical result is plotted with black dashes.

We then add those energy shifts to the energy levels that have been calculated to get Figure 9a. For this purpose we confine the particle to 13 nm, and we use a lattice constant of 0.5 nm. In Kwant we do this by specifying a system shape and a lattice constant parameter. We could have used different values here, as long as they are the same in the two calculations that we are comparing.

Secondly, we simulate Eq.(84) using the combined computational method, as explained in Section 2.1. If the implementation of Kwant in the combined computational method is correct, the two calculations should have the same result. In Figure 9b we see the result of the comparison. The calculation that we did by adding the energy shifts is plotted with blue lines, and the calculation that we did with the combined computational method is plotted with black dashes. There are no significant differences between these two calculations, indicating that Kwant is implemented correctly in the combined computational method.

3.5 APPLICATION TO THE $k \cdot p$ HAMILTONIAN

In the previous sections of this chapter we have seen that the computational method behaves as expected. When tested on the toy model Hamiltonian, only one eigenvalue has a significant error, and it is the eigenvalue that is predicted to be wrong because of coupling with a higher LL. The test case Hamiltonian is very sparse and diagonally dominant, and subsequent LLs increase in energy. One may question whether the $k \cdot p$ Hamiltonian that we will use for the final simula-

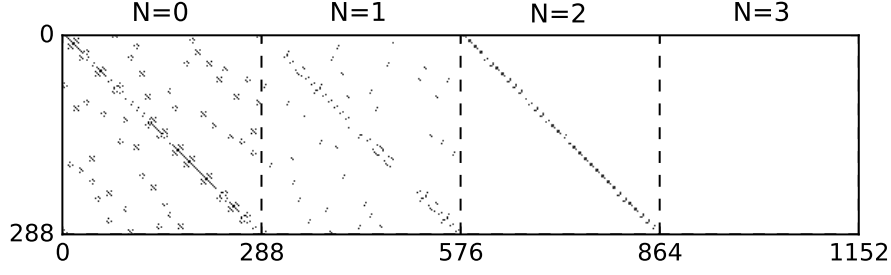


Figure 4: Plot of the first four LL subblocks of the first row of a simulated $k \cdot p$ Hamiltonian, for a magnetic field strength of 2.5 T. The white space denotes zero valued matrix elements, and the black dots are non-zero valued matrix elements. N denotes the LL.

tion is also well suited to be approximated by truncation. We will now qualitatively discuss this question.

First we make a plot of the first four LL subblocks of the first row of a simulated Hamiltonian, we do this for a magnetic field strength of 2.5 T. Because of the order of the Kronecker products in the computational code, the outermost substructure of the final Hamiltonian will be the LLs. We are using an 8×8 Hamiltonian, with a system length of 18 nm, and a lattice constant of 0.5 nm, so we expect the size of one LL subblock to be 288 elements. The plot can be seen in Figure 4.

There is no color map because the colors would be indiscernible without zooming in. The white space denotes zero valued matrix elements, and the black dots are non-zero valued matrix elements. N denotes the LL. We cannot see this in the plot, but the values of the matrix elements in the first block are highest in magnitude, and the values decrease in magnitude for higher LLs.

We see that the blocks become more sparse the further away they are from the diagonal, and that all values in the fourth and further blocks are zero. This means that there is coupling between LLs N and $N+1$ and also between LLs N and $N+2$. There is no coupling between LLs N and $N+3$ and further. We could also have deduced this from the fact that the Hamiltonian is only linear and quadratic in k , and not cubic or of higher degree in k .

Another point that is important to remark is that just like in the toy model, because of the equal spacing between LLs, subsequent LLs will have higher energies. If we would define some dimensionless parameter that describes the relative magnitude of the coupling, this parameter would decrease in magnitude as we progress further down the diagonal. This qualitative discussion shows us that it is reasonable to approximate the eigenvalues of the $k \cdot p$ Hamiltonian by using our computational method, as long as we simulate enough LLs.

SIMULATION RESULTS

We have done simulations in both the trivial and inverted regime. For the trivial regime we have layers of GaSb/InAs/AlSb with widths of respectively 3 nm, 5 nm and 5 nm. For the inverted regime we have layers of AlSb/InAs/GaSb/InAs with layer widths of respectively 5 nm, 12.5 nm, 5 nm and 5 nm. We use a standard semiconductor 8×8 $k \cdot p$ Kane Hamiltonian. The Hamiltonian is obtained from Nichele et al. [17] and the code to generate the Hamiltonian was contributed by Rafal Skolasinski. All parameters values are retrieved from Halvorsen et al. [8], except for the kappa parameter which comes from Lawaetz [12].

First we do a simulation with equal intervals in B , from which we obtain a Landau fan diagram. We then perform another simulation with equal intervals in $1/B$. From this we analyze the magnetic oscillations in the DOS near the Fermi energy, which is an approximation to the SdH oscillations. We do this for a range of electron concentrations, and thus for a range of Fermi energies. We look for beatings in the oscillations, which are caused by the interplay of the LL spacing, Rashba effect and Zeeman effect [5, 10].

4.1 LANDAU FANS IN THE TRIVIAL AND INVERTED REGIMES

In Figure 5 we can see the Landau fan diagram that we obtain from the simulation in the trivial regime. The most obvious features are the equal spacing in energy at constant B values, and the spin splitting of the LLs. We also see that there are gaps in the energy level data, which is a result of the truncation. This will limit our ability to analyze the magnetic oscillations for small magnetic fields and large carrier concentrations.

One interesting feature that is the most pronounced at the uppermost LLs is that the LLs are nonlinear in B . We can explain this with the fact that the in-plane dispersion is non-parabolic [23]. We can clearly see that this is the trivial regime, because of the approximately 50 meV gap between the electron and hole band.

Now we do a test by comparing the Landau fan with a dispersion diagram for zero magnetic field. In Eq.(25) we see that at zero magnetic field the momentum operators are replaced by zero. Because of this, the zero magnetic field points in the Landau fan must agree with the dispersion band edges at zero magnetic field. In Figure 6a we see a dispersion diagram that was made using Kwant. We can see that the dispersion diagram and the Landau fan diagram agree.

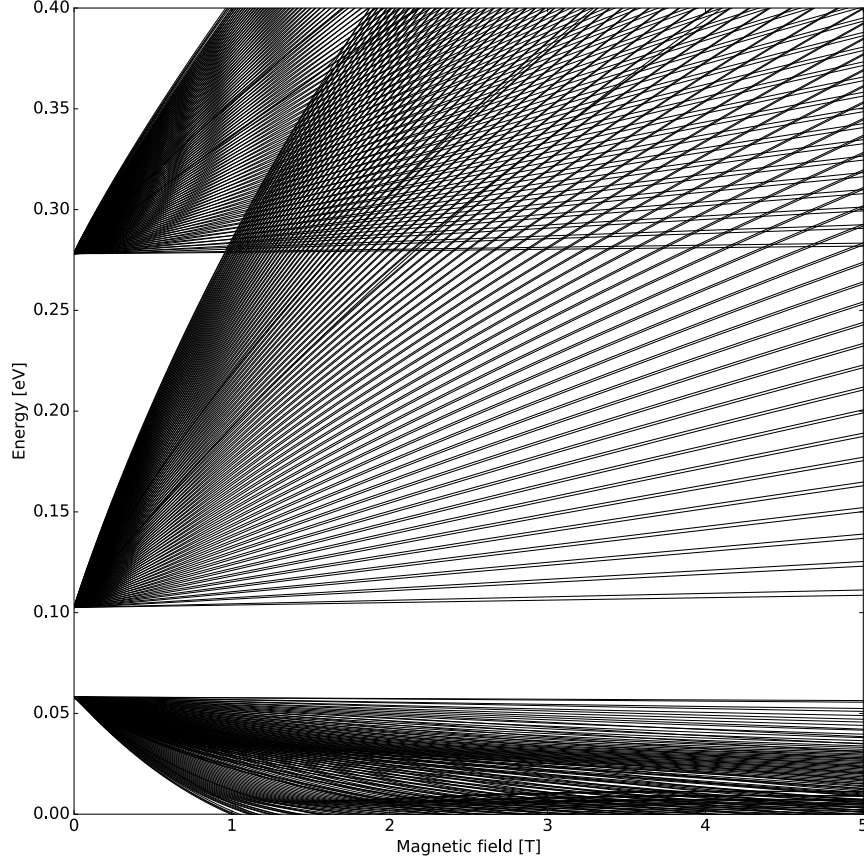
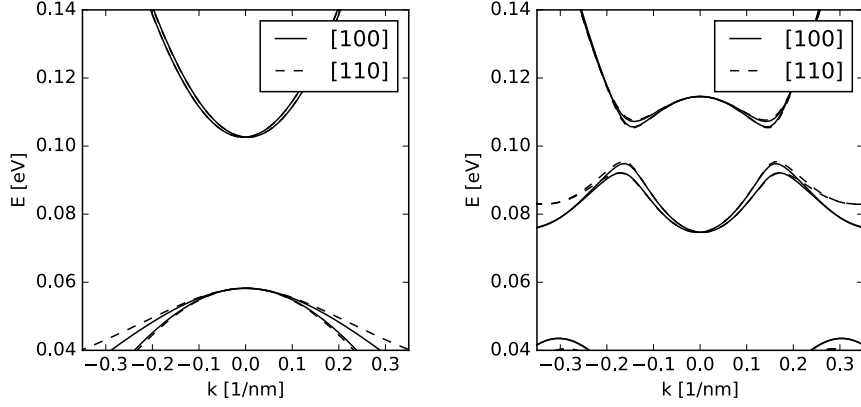


Figure 5: Landau fan diagram of the GaSb/InAs/AlSb heterostructure, simulated in the trivial regime.

Figure 6b shows a plot of the dispersion relation in the inverted regime. We observe that the hole band has been shifted upwards into the electron band. This is what makes this an inverted regime, or 2DTI phase. We can also see in the diagram why we call this an inverted regime. If we look at small k , we see that the band structure of the conduction and valence band have been inverted there.

In Figure 7 we see the Landau fan of the inverted regime. First it must be remarked that there are some graphical artifacts because the data is plotted as points instead of lines. As we expect from our discussion of the dispersion diagram, we see that the hole band has moved into the electron band. The Landau fans are also inverted around the band gap. If we look at the band gap around 0.1 eV, we see a state moving from the hole band into the electron band, and vice versa. These are the edge protected states of the 2DTI phase. The dispersion diagram and the Landau fan agree on energy values for zero k .



(a) Simulated dispersion in the trivial regime. (b) Simulated dispersion in the inverted regime.

Figure 6: Simulated dispersion diagrams for the trivial and normal regimes. [100] denotes the dispersion in the x-direction and [110] denotes the dispersion in the y-direction.

4.2 MAGNETIC OSCILLATIONS IN THE TRIVIAL REGIME

In the trivial regime, we calculate the DOS near the Fermi energy from the LLs using a Gaussian broadening [23]:

$$D(E_F, B) = G \sum_i \frac{1}{\sqrt{2\pi}\Gamma} \exp\left(-\frac{(E_F - E_i)^2}{2\Gamma^2}\right). \quad (86)$$

The degeneracy per unit area of the spin-split LLs is [23]

$$G = \frac{eB}{h}. \quad (87)$$

Γ is a phenomenological broadening parameter that represents the imperfection of the LLs because of scattering and impurities [3]. The E_i are the calculated energy values for a certain magnetic field strength. The Fermi wave vector equals

$$k_F = \sqrt{2\pi n}, \quad (88)$$

where n is the electron concentration per unit area. Because the dispersion is not parabolic and the effective mass of the sub-band is generally not the same as the bulk value, we calculate the Fermi energy from the Fermi wave vector using the dispersion that is plotted in Figure 6a. For this purpose we do a polynomial fit, to get a polynomial P . Because the polynomial also contains a zeroth order term for the bottom of the conduction band E_c , the Fermi energy is

$$E_F = P(k_F). \quad (89)$$

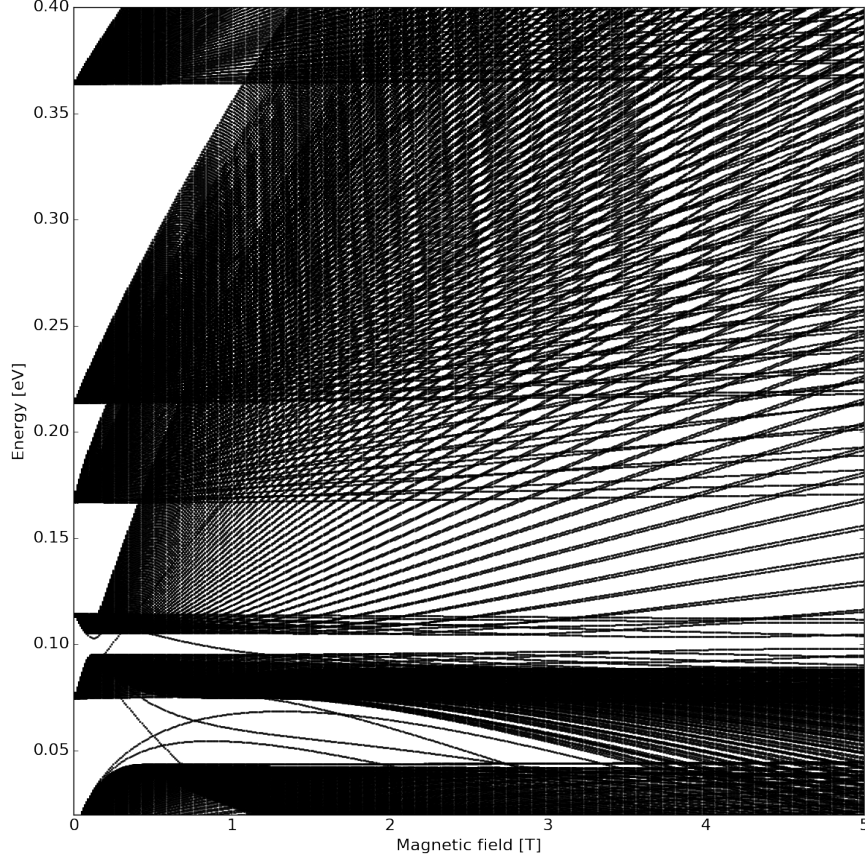


Figure 7: Landau fan diagram of the GaSb/InAs/AlSb heterostructure , simulated in the inverted regime.

We calculate the DOS near the Fermi energy for electron concentrations ranging from $0-10 \cdot 10^{15} \cdot \text{m}^{-2}$. We do this for two different broadenings, 0.3 meV and 0.75 meV.

In Figure 8a and Figure 8b we can see the oscillations in the DOS for a broadening of 0.3 meV, and in Figure 8c and Figure 8d for a broadening of 0.75 meV . The electron concentration for these figures is $4 \cdot 10^{15} \cdot \text{m}^{-2}$. The figures on the left hand side have the magnetic field strength on the horizontal axis, the figures on the right hand side are plotted against the reciprocal of the magnetic field strength. From the plots we see that the oscillations are quasi periodic in $1/B$. We can clearly see a beating in the oscillations for the broadening of 0.3 meV. At 0.75 meV only a relatively very small beating is visible.

Beatings in signals originate from a superposition of two waves with slightly different frequencies. The beating that we observe in magnetic oscillations results from a frequency difference between the oscillations of the two different spin states [5]. In general, the spin states do not have equal charge densities [23], but the sum of the two densities equals the total electron density

$$n = n_+ + n_- . \quad (90)$$

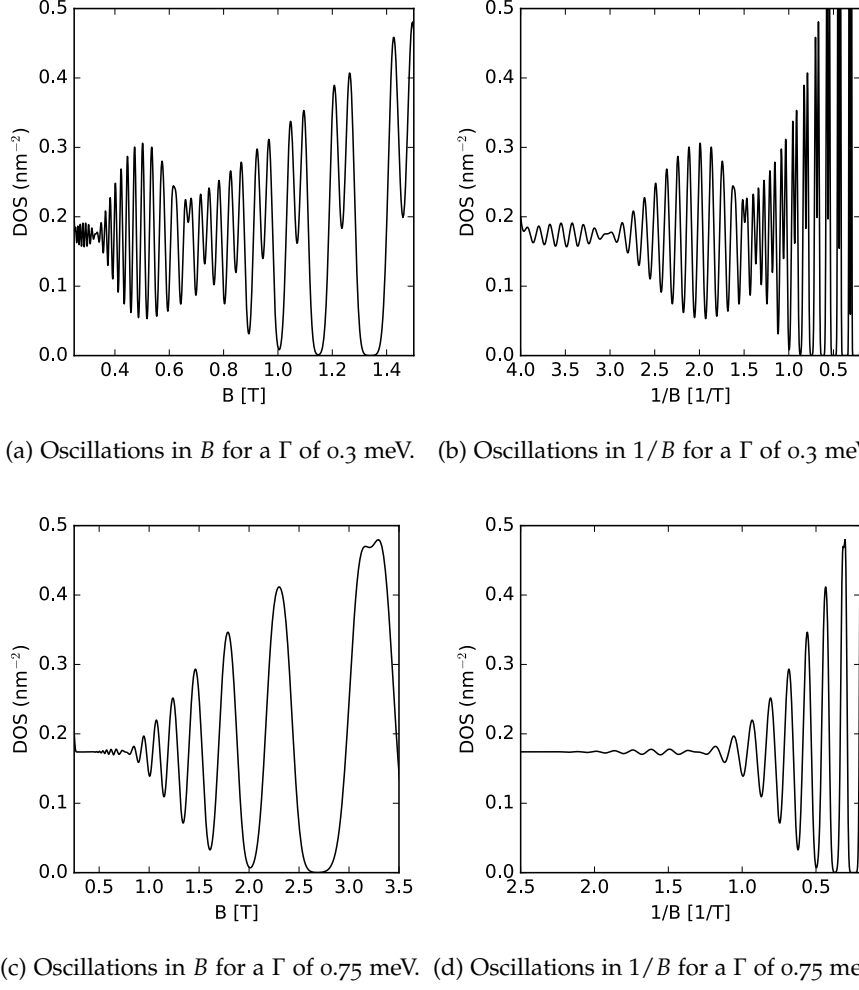


Figure 8: Magnetic oscillations in the DOS near the Fermi energy for two broadenings and an electron concentration of $4 \cdot 10^{15} \cdot \text{m}^{-2}$.

The frequency of the magnetic oscillation for each spin state is [23]

$$f_{\pm} = \frac{n_{\pm} h}{e}. \quad (91)$$

The distribution between the two densities does not have to be the same for every total density. Therefore, we will look at the average of the two frequencies, so that we can use the total charge density:

$$\frac{f_{+} + f_{-}}{2} = \frac{nh}{2e} \quad (92)$$

We now do a FFT of the oscillations in $1/B$ for a range of electron concentrations. The FFTs for all concentrations are plotted in one figure, where the magnitude of the FT is in arbitrary units. We also plot a dashed line that equals the average frequency from Eq.(92) as a function of total electron concentration. The line should intersect at

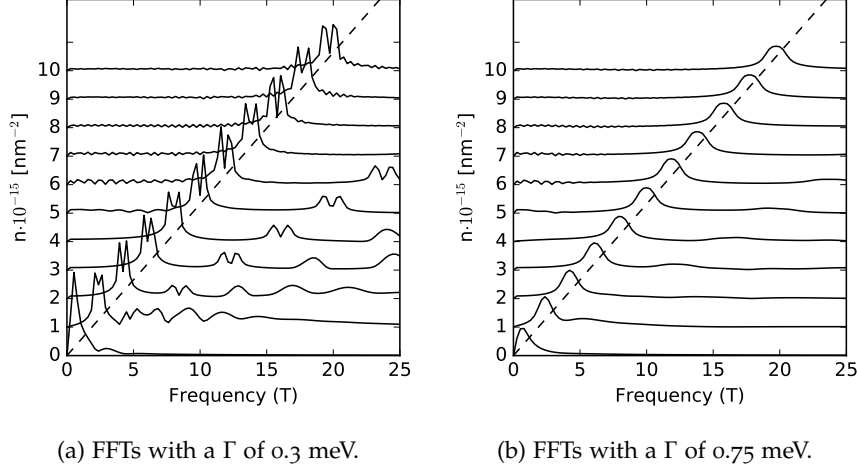


Figure 9: FFTs in arbitrary units of the magnetic oscillations in $1/B$, for a range of carrier concentrations and two different broadenings. The dashed line represents the theoretical frequencies from Eq.(92).

the bottom of the middle of the two frequency peaks. We can see the results in Figure 9.

In the first figure we see the plot for a broadening of 0.3 meV. there are two distinct peaks, which are the peaks of the two spin states, and which cause the beating that is visible in Figure 8. For zero concentration the two frequencies are not separated. We see that for low carrier concentrations the line fits to the middle of the peaks. For higher concentrations there is a small deviation. We can also observe small peaks at the harmonics of the two frequencies.

In the second figure we see the FFTs for a broadening of 0.75 meV. As we would expect from the oscillations in Figure 8, the two frequencies are not clearly separated. However, there is not one distinct peak, which is why only a slight beating is visible in Figure 8.

4.3 POSSIBILITIES FOR IMPROVEMENT AND FURTHER RESEARCH

For further research it is interesting to also investigate the behavior of the magnetic oscillations for larger electron concentrations. However, this is not possible with the amount of LLs that we simulated. This is because for large concentrations and small magnetic field strengths, the Fermi energy is inside the data gap that results from the truncation.

Furthermore, instead of calculating the Fermi energy from a polynomial fit to the dispersion, we can also calculate it from an iterative solution of the integral equation that relates the total electron density to the Fermi energy [23]. This way, the Fermi energy is B dependent and moves in a jagged pattern from LL to LL [23]. A comparison of these two methods is interesting to explore in further research.

For the Fourier analysis we limited ourselves to the trivial regime. It is interesting to also do this analysis in the inverted regime, and investigate the behavior of the beatings in this regime.

CONCLUSION

We developed a computational method that can efficiently simulate LLs. This is a valuable tool for both theoretical and experimental research. The method has first been tested on an analytically solvable toy model that includes the Rashba and the Zeeman effect. The computational method behaves as expected, and the approximation by truncation only causes significant errors in the few topmost LLs.

We then used this tool to simulate LLs of a GaSb/InAs/AlSb heterostructure in both the trivial and inverted regimes using an 8×8 Kane Hamiltonian in the standard semiconductor $k \cdot p$ model. As a test, we have compared the results with a dispersion diagram that was calculated using Kwant. The simulation in the trivial regime shows us a separation between the electron and hole bands. In the inverted regime we observe a shift of the hole band into the electron band, which causes an invertedness around the gap. We also see an electron state moving into the hole band, and vice versa.

Finally, we calculated the magnetic oscillations of the electronic DOS near the Fermi energy in the trivial regime. We did this for different broadenings and electron concentrations. We calculated the Fermi energies by doing a polynomial fit to the dispersion. As expected, the oscillations are quasi periodic in $1/B$. We observe a clear beating for a broadening of 0.3 meV. For a broadening of 0.75 meV, the beating has almost disappeared.

We further analyzed the oscillations by performing a FFT in $1/B$. For a broadening of 0.3 meV we see two distinct peaks that cause the beating in the magnetic oscillations. These two frequencies belong to the two different spin states of the electrons. For a broadening of 0.7 meV there is no clear distinction between the two frequencies anymore. We also plotted the Fourier spectrum against a line that represents the theoretically expected average frequency. The Fourier spectrum shows only a small deviation from this line.

For further research it would be interesting to also investigate the magnetic oscillations for larger electron concentrations, we can do this by simulating more LLs. With the analysis of the magnetic oscillations, we have limited ourselves to the trivial regime. For further research it is interesting to also do the Fourier analysis in the inverted regime.

THE KDOTP HAMILTONIAN

$$H = \begin{pmatrix} T & 0 & -\frac{1}{\sqrt{2}}Pk_+ & \sqrt{\frac{2}{3}}Pk_z & \frac{1}{\sqrt{6}}Pk_- & 0 & -\frac{1}{\sqrt{3}}Pk_z & -\frac{1}{\sqrt{3}}Pk_- \\ 0 & T & 0 & -\frac{1}{\sqrt{6}}Pk_+ & \sqrt{\frac{2}{3}}Pk_z & \frac{1}{\sqrt{2}}Pk_- & -\frac{1}{\sqrt{3}}Pk_+ & \frac{1}{\sqrt{3}}Pk_z \\ -\frac{1}{\sqrt{2}}k_-P & 0 & U+V & -\bar{S}_- & R & 0 & \frac{1}{\sqrt{2}}\bar{S}_- & -\sqrt{2}R \\ \sqrt{\frac{2}{3}}k_zP & -\frac{1}{\sqrt{6}}k_-P & -\bar{S}_-^\dagger & U-V & C & R & \sqrt{2}V & -\sqrt{\frac{3}{2}}\tilde{S}_- \\ \frac{1}{\sqrt{6}}k_+P & \sqrt{\frac{2}{3}}k_zP & R^\dagger & C^\dagger & U-V & \bar{S}_+^\dagger & -\sqrt{\frac{3}{2}}\tilde{S}_+ & -\sqrt{2}V \\ 0 & \frac{1}{\sqrt{2}}k_+P & 0 & R^\dagger & \bar{S}_+ & U+V & \sqrt{2}R^\dagger & \frac{1}{\sqrt{2}}\bar{S}_+ \\ -\frac{1}{\sqrt{3}}k_zP & -\frac{1}{\sqrt{3}}k_-P & \frac{1}{\sqrt{2}}\bar{S}_-^\dagger & \sqrt{2}V & -\sqrt{\frac{3}{2}}\tilde{S}_+^\dagger & \sqrt{2}R & U-\Delta & C \\ -\frac{1}{\sqrt{3}}k_+P & \frac{1}{\sqrt{3}}k_zP & -\sqrt{2}R^\dagger & -\sqrt{\frac{3}{2}}\tilde{S}_-^\dagger & -\sqrt{2}V & \frac{1}{\sqrt{2}}\bar{S}_+^\dagger & C^\dagger & U-\Delta \end{pmatrix}$$

For more information about this Hamiltonian, and its parameters, please see the supplemental material in [17].

BIBLIOGRAPHY

- [1] Neil W Ashcroft and N Mermin. *Solid State Physics*. Cengage Learning, Inc, 1976, p. 848.
- [2] D.D Awschalom, D Loss, and N Samarth. *Semiconductor Spintronics and Quantum Computation*. Springer Science & Business Media, 2013, p. 311.
- [3] F. Azfar. “Cyclotron Resonance.” In: *Oxford University* (2009), pp. 71–90. URL: http://www2.physics.ox.ac.uk/sites/default/files/BandMT{_}09.pdf.
- [4] Yu a Bychkov and E I Rashba. “Oscillatory effects and the magnetic susceptibility of carriers in inversion layers.” In: *Journal of Physics C: Solid State Physics* 17.33 (1984), pp. 6039–6045. ISSN: 0022-3719. DOI: [10.1088/0022-3719/17/33/015](https://doi.org/10.1088/0022-3719/17/33/015). URL: <http://stacks.iop.org/0022-3719/17/i=33/a=015?key=crossref.2f8159f54a3070499f32bac53e23f947>.
- [5] L.J. Cui, Y.P. Zeng, Y. Zhang, W.Z. Zhou, L.Y. Shang, T. Lin, and J.H. Chu. “Beating patterns in the Shubnikov-de Haas oscillations originated from spin splitting in In_{0.52}Al_{0.48}As/In_{0.65}Ga_{0.35}As heterostructures: Experiment and calculation.” In: *Physica E: Low-dimensional Systems and Nanostructures* 83 (2016), pp. 114–118. ISSN: 13869477. DOI: [10.1016/j.physe.2016.04.028](https://doi.org/10.1016/j.physe.2016.04.028). URL: <http://linkinghub.elsevier.com/retrieve/pii/S1386947716302983>.
- [6] David J. Griffiths. *Introduction to Quantum Mechanics*. 1995. DOI: [10.1038/155772b0](https://doi.org/10.1038/155772b0). URL: http://pdfserv.aip.org/PHTOAD/vol{_}48/iss{_}3/94{_}1.pdf.
- [7] Christoph W Groth, Michael Wimmer, Anton R Akhmerov, and Xavier Waintal. “Kwant : a software package for quantum transport.” In: (2014), pp. 1–19.
- [8] E. Halvorsen, Y. Galperin, and K. Chao. “Optical transitions in broken gap heterostructures.” In: *Physical Review B* 61.24 (2000), pp. 16743–16749. ISSN: 0163-1829. DOI: [10.1103/PhysRevB.61.16743](https://doi.org/10.1103/PhysRevB.61.16743). URL: <http://link.aps.org/doi/10.1103/PhysRevB.61.16743>.
- [9] Ivan Knez, Rui Rui Du, and Gerard Sullivan. “Evidence for helical edge modes in inverted InAs/GaSb quantum wells.” In: *Physical Review Letters* 107.13 (2011), pp. 1–5. ISSN: 00319007. DOI: [10.1103/PhysRevLett.107.136603](https://doi.org/10.1103/PhysRevLett.107.136603).

- [10] Takaaki Koga, Toru Matsuura, Bastien Faniel, Satofumi Souma, Shunsuke Mineshige, Yoshiaki Sekine, and Hiroki Sugiyama. "Beating Analysis of Shubnikov de Haas Oscillation in In_{0.53}Ga_{0.47}As Double Quantum Well toward Spin Filter Applications." In: *IE-ICE Transactions on Electronics* E95.C.5 (2012), pp. 770–776. ISSN: 0916-8524. DOI: [10.1587/transele.E95.C.770](https://doi.org/10.1587/transele.E95.C.770).
- [11] Herbert Kroemer. "The 6.1 Å family (InAs, GaSb, AlSb) and its heterostructures: A selective review." In: *Physica E: Low-Dimensional Systems and Nanostructures*. 2004. ISBN: 1386-9477. DOI: [10.1016/j.physe.2003.08.003](https://doi.org/10.1016/j.physe.2003.08.003).
- [12] P. Lawaetz. "Valence-band parameters in cubic semiconductors." In: *Physical Review B* 4.10 (1971), pp. 3460–3467. ISSN: 01631829. DOI: [10.1103/PhysRevB.4.3460](https://doi.org/10.1103/PhysRevB.4.3460).
- [13] J. Luo, H. Munekata, F. F. Fang, and P. J. Stiles. "Observation of the zero-field spin splitting of the ground electron subband in gasb-inas-gasb quantum wells." In: *Physical Review B* 38.14 (1988), pp. 10142–10145. ISSN: 01631829. DOI: [10.1103/PhysRevB.38.10142](https://doi.org/10.1103/PhysRevB.38.10142).
- [14] Lorenz Meier, Gian Salis, Ivan Shorubalko, Emilio Gini, Silke Schön, and Klaus Ensslin. "Measurement of Rashba and Dresselhaus spin-orbit magnetic fields." In: *Nature Physics* 3. September (2007), pp. 650–654. ISSN: 1745-2473. DOI: [10.1038/nphys675](https://doi.org/10.1038/nphys675). URL: <http://arxiv.org/abs/0709.2509><http://www.nature.com/doi/10.1038/nphys675>.
- [15] Joel E Moore. "The birth of topological insulators." In: *Nature* 464.7286 (2010), pp. 194–8. ISSN: 1476-4687. DOI: [10.1038/nature08916](https://doi.org/10.1038/nature08916). URL: <http://www.ncbi.nlm.nih.gov/pubmed/20220837>.
- [16] Fabrizio Nichele et al. "Edge Transport in the Trivial Phase of InAs/GaSb." In: (2015). ISSN: 1367-2630. DOI: [10.1088/1367-2630/18/8/083005](https://doi.org/10.1088/1367-2630/18/8/083005). URL: <http://arxiv.org/abs/1511.01728><http://dx.doi.org/10.1088/1367-2630/18/8/083005>.
- [17] Fabrizio Nichele et al. "Giant spin-orbit splitting in inverted InAs/GaSb double quantum wells." In: 1 (2016), pp. 1–10. URL: <http://arxiv.org/abs/1605.01241>.
- [18] Vlad S Pribiag, Arjan J A Beukman, Fanming Qu, Maja C Cassidy, Christophe Charpentier, Werner Wegscheider, and Leo P Kouwenhoven. "Edge-mode Superconductivity in a Two Dimensional Topological Insulator." In: (2014).
- [19] Fanming Qu et al. "Electric and Magnetic Tuning between the Trivial and Topological Phases in InAs/GaSb Double Quantum Wells." In: *Physical Review Letters* (2015). ISSN: 10797114. DOI: [10.1103/PhysRevLett.115.036803](https://doi.org/10.1103/PhysRevLett.115.036803).
- [20] Christopher Schierholz. *Rashba Spin-Orbit Interaction in Low and High Magnetic Fields*. Cuvillier Verlag, 2005.

- [21] D Schoenberg. *Magnetic Oscillations in Metals*. Cambridge University Press, 1984.
- [22] Tim Oliver Stadelmann. “Antidot Superlattices in {InAs–GaSb} Double Heterostructures: transport studies.” In: (2006). URL: <http://timstadelmann.de/thesisbod.pdf>.
- [23] R Winkler. “Spin-Orbit Coupling Effects in Two-Dimensional Electron and Hole Systems.” In: (2003). DOI: [10.1007/b13586](https://doi.org/10.1007/b13586).